The influence of deep jets on Jupiter's weather layer in a 1.5-layer shallow-water model

Stephen I. Thomson[1]*

[1]College of Engineering, Mathematics and Physical Sciences, University of Exeter, Exeter, EX4 4QF, UK

Correspondence
Dr Stephen I. Thomson, College of Engineering, Mathematics and Physical Sciences, University of Exeter, Exeter, EX4 4QE, United Kingdom
Email: stephen.i.thomson@gmail.com

Funding information

The depth of the jet streams seen in Jupiter's outer weather layer has long been debated, with alternative suggestions of confinement to the weather layer, and extensions deep into the planet being considered. Interpretation of measurements from NASA's Juno probe have suggested that the weather-layer jets do extend deep into the planet down to depths of $O(3,000km)$. However this relies on the assumption that the jet profile does not change its spatial structure with depth, which may not be the case. In this work we consider a simple 1.5-layer shallow-water model of Jupiter-like jet streams, with prescribed deep jets in the lower layer, and look at the parameters affecting the strength of the coupling between the layers. We find the value of the Rossby deformation scale, L_D to be particularly important, not just in setting the magnitude of variations in layer depth, but also in dictating the effectiveness of radiative damping. We also find the radiative damping timescales, the energy injection rate, and the spacing of the deep jets to be important. We combine these findings into our best-guess simulations of the real-Jupiter and find that the low latitudes are relatively uncoupled between the layers, with the high latitudes being more tightly coupled. These effects can be tied to the smallness of Jupiter's L_D and the effectiveness of radiative damping as a coupling mechanism. These simulations do, however, produce equatorial subrotation, and eddy-momentum fluxes unlike those on the real planet. It may be, therefore, that

This article has been accepted for publication and undergone full peer review but has not been through the copyediting, typesetting, pagination and proofreading process, which may lead to differences between this version and the Version of Record. Please cite this article as doi: 10.1002/qj.3755

spatially-varying forcing, and very long radiative damping timescales are required for this model to be more Jupiter-like.

KEYWORDS
Jet streams, Giant planets, Shallow-water equations,

1 | INTRODUCTION

Jupiter's outer atmosphere is famous for its multiple jet streams, which can be visualised via tracking of visible cloud features (Porco et al., 2003). These jet streams are remarkably steady in time, and are also remarkably straight, in that they run almost along lines of constant latitude. The reasons for the cloud-level jet streams having these properties are still debated.

One significant question regarding these jet streams, which may help to explain the cloud-level properties, is how deep the winds at cloud level penetrate into the planet. The vertical structure of Jupiter's atmosphere begins with a statically-stable, moist convecting 'weather layer', which can be thought of as extending from the tropopause to the bottom of the water-cloud condensation level, at $O(10)$ bars. Beneath this layer is a significantly deeper region of neutrally-stable convection, the 'dry-convection layer' driven by the escape of Jupiter's internal heat flux. Estimates from interior models have this layer extending down to the transition where hydrogen becomes so hot and dense that it becomes metallic (see e.g. figure 6 of Guillot (2005)).

A vast array of papers have described jet streams being formed in the dry-convection layer (see e.g. Heimpel et al., 2005; Jones and Kuzanyan, 2009, and references therein), or in the weather-layer (see e.g. Williams, 2003; Schneider and Liu, 2009), but relatively few have considered the interaction between these two layers. The exceptions to this rule mostly fall into the category of so-called 1.5-layer models, where the active upper layer represents the weather-layer, and the time-constant 'half-layer' represents high-inertia flow in the dry convection layer (Dowling and Ingersoll, 1989; Thomson and McIntyre, 2016), with additional recent work starting to look at this interaction in modified deep-convection models (Heimpel et al., 2016). Despite these exceptions, a systematic exploration of the coupling between these two layers has, so far, not been documented. This work aims to begin to fill this gap.

In terms of observational constraints, NASA's Juno probe has recently been measuring Jupiter's gravity field to high precision, and these observations have been put through inverse models to reconstruct the depth of the jet streams (Kaspi et al., 2018). The study of Kaspi et al. (2018) has suggested that the jet streams extend down to $\sim 3,000$km, with this depth varying in latitude (see their figure 4b), meaning that the jets extend well below the bottom of the weather layer and into the dry-convection layer. In making this estimate, Kaspi et al. (2018) assume that the spatial profile of the jet streams stays constant with depth, with the amplitude decaying. This simplifying assumption, and other aspects of this method, have recently been challenged by Kong et al. (2018), who suggest that the Juno's measurements are consistent with many possible deep-wind profiles that are not necessarily the same as those at cloud level. There are, of course, physical constraints on what these deep jet profiles can be, including possible constraints from Juno's forthcoming time-varying magnetic field measurements Duer et al. (2019). Despite these constraints, and until further measurements are available, some uncertainty remains.

Without considering the validity of either approach to interpreting Juno's measurements, one possibility for breaking this degeneracy is to consider what the factors are that affect the coupling between the jets in the weather-layer and those those in the dry-convection layer. For example, consider that jet streams are able to form in Jupiter's

convective interior, as modelled by e.g. Heimpel et al. (2016) and references therein. The question could then be asked if the jet streams in the weather-layer, with their significantly lower mass, are tightly coupled to those in the deep layer? Or is the coupling weak, meaning that a given deep wind profile has no impact on the weather-layer?

Previous studies that have considered both layers simultaneously have mostly focused on finding the velocities in the deep layer from observing the motion around Jupiter's Great Red Spot (Dowling and Ingersoll, 1988, 1989; Shetty et al., 2007; Shetty and Marcus, 2010; Marcus and Shetty, 2011). In the simulations conducted by Dowling and Ingersoll (1989), they use their derived deep flow measurements as the velocity profile in their half-layer, and use a Rayleigh-drag to bring the velocity profiles in both layers close to matching. The problem with this approach is that they do not justify the physical mechanisms for such a drag. In Thomson and McIntyre (2016) it was found that, without invoking such a drag a priori, moist-convection could play a similar role, making the weather-layer's jet profile closely match that in the deep layer under a range of circumstances. All of these papers, however, only consider a narrow range of latitudes, and so the global picture is still missing.

To address these problems we use a global shallow-water model with 1.5 layers. Shallow-water dynamics is well justified for Jupiter's weather layer, whose depth is a small fraction of Jupiter's radius, and has been used in previous studies of Jupiter by Cho and Polvani (1996); Cho et al. (2001); Scott and Polvani (2007). Separate from the shallow-water approximations, the ratio of masses for Jupiter's dry-convective interior and weather layer is small enough that the 1.5-layer approximation is well-justified (see section 1.3.2 of Thomson, 2015, for further details). Given that the model is significantly simplified compared with Jupiter itself, we take the approach of looking at the factors and parameters that affect the vertical coupling between the two layers, and comment on which we deem to be most applicable to Jupiter.

The structure of the paper is as follows - section 2 derives the 1.5-layer model equations, section 3 gives some scaling arguments for the regimes of strong and weak coupling, section 4 describes the results of our numerical simulations, section 5 attempts to find the most realistic combination of our model parameters, and section 6 discusses the results and draws conclusions.

2 | DERIVATION OF THE 1.5-LAYER SHALLOW-WATER MODEL WITH RADIATIVE DAMPING

To justify the use of our global 1.5-layer shallow-water model, we begin by deriving the equations for the more-familiar 2-layer shallow-water model, and then making the approximations necessary for 1.5-layer dynamics.

2.1 | Formulation of the 2-layer model

We denote the upper layer as layer-1, and the lower layer as layer-2. A vertical section of the model is shown in figure 1. The depth of fluid in each layer is

$$h_1(\lambda, \phi, t) = H_1 - \eta(\lambda, \phi, t) \tag{1}$$

$$h_2(\lambda, \phi, t) = H_2 + \eta(\lambda, \phi, t), \tag{2}$$

where λ is longitude, ϕ is latitude and t is time. By formulating the height variables in this way, we have built into the equations that $h_1 + h_2$ is fixed in time and space, consistent with a rigid-lid approximation. Such a rigid-lid can be thought of as representing the bounding of the weather-layer above by the tropopause. We have chosen the rigid-lid

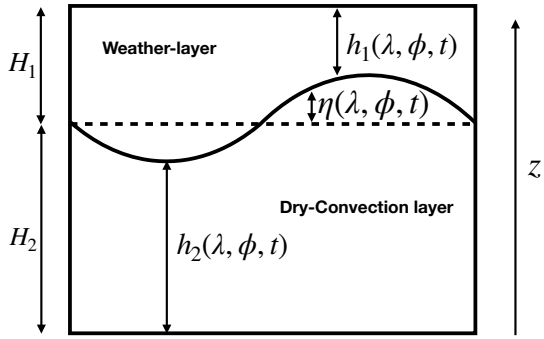

FIGURE 1 Representation of the vertical structure of the two-layer model, with depth definitions in equations (1) and (2).

approximation as height variations at the upper boundary are small, consistent with $g \gg g'$ (see e.g. section 3.2.1 of Vallis (2017)), and imposing a rigid lid prevents us from having to choose a value for the external Rossby-deformation scale as well as the internal value, denoted in this paper as L_D, which keeps our investigation simple.

To calculate the pressure within each layer, we assume hydrostatic equilibrium in both layers, and that pressure is continuous across the interface. In the upper layer we have $\partial p_1 / \partial z = -g\rho_1$, which can be integrated in the z direction to give

$$p_1(\lambda, \phi, z, t) = p_0(\lambda, \phi, t) - g\rho_1 z, \tag{3}$$

where p_0 is an arbitrary function of (λ, ϕ, t).

At $z = H_1 + H_2$ there is the rigid lid, which we account for by setting $p_1(\lambda, \phi, z = H_1 + H_2, t) = \mathcal{P}(\lambda, \phi, t)$, where $\mathcal{P}$ is the pressure exerted on the fluid by the rigid lid. We can substitute this into (3), and get that

$$\mathcal{P}(\lambda, \phi, t) = p_0(\lambda, \phi, t) - g\rho_1(H_1 + H_2), \tag{4}$$

meaning that

$$p_1(\lambda, \phi, z, t) = \mathcal{P}(\lambda, \phi, t) + g\rho_1(H_{tot} - z), \tag{5}$$

where $H_{tot} = H_1 + H_2$.

In the lower layer we have $\partial p_2 / \partial z = -g\rho_2$, which is then integrated to be

$$p_2(\lambda, \phi, z, t) = P_0(\lambda, \phi, t) - g\rho_2 z, \tag{6}$$

where P_0 is also an arbitrary function of (λ, ϕ, t). Pressure is continuous at the interface, meaning that

$$\mathcal{P}(\lambda, \phi, t) + g\rho_1(H_{tot} - (H_2 + \eta)) = P_0(\lambda, \phi, t) - g\rho_2(H_2 + \eta). \tag{7}$$

Re-arranging for P_0 gives

$$P_0(\lambda,\phi,t) = \mathcal{P}(\lambda,\phi,t) + g\rho_1(H_{tot} - (H_2+\eta)) + g\rho_2(H_2+\eta), \tag{8}$$

meaning that

$$p_2(\lambda,\phi,z,t) = \mathcal{P}(\lambda,\phi,t) + g\rho_1(H_{tot} - (H_2+\eta)) + g\rho_2(H_2+\eta-z). \tag{9}$$

Considering now the momentum equations for the two shallow-water layers, we have

$$\frac{D_1\vec{u_1}}{Dt} + \vec{f}\times\vec{u_1} = -\frac{1}{\rho_1}\vec{\nabla}_H p_1(\lambda,\phi,z,t) \tag{10}$$

$$\frac{D_2\vec{u_2}}{Dt} + \vec{f}\times\vec{u_2} = -\frac{1}{\rho_2}\vec{\nabla}_H p_2(\lambda,\phi,z,t), \tag{11}$$

where $\vec{\nabla}_H = ((1/a\cos\phi)\partial/\partial\lambda, (1/a)\partial/\partial\phi, 0)$ is the horizontal gradient operator. In subsequent equations this will be abbreviated to $\vec{\nabla}$. Also in this equation is the Coriolis vector $\vec{f} = (0,0,f)$, where $f = 2\Omega\sin\phi$ is the Coriolis parameter. Substituting in expressions (5) and (9) gives

$$\frac{D_1\vec{u_1}}{Dt} + \vec{f}\times\vec{u_1} = -\frac{1}{\rho_1}\vec{\nabla}\mathcal{P}(\lambda,\phi,t) \tag{12}$$

$$\frac{D_2\vec{u_2}}{Dt} + \vec{f}\times\vec{u_2} = -\frac{1}{\rho_2}\vec{\nabla}\mathcal{P}(\lambda,\phi,t) - \frac{g(\rho_2-\rho_1)}{\rho_2}\vec{\nabla}\eta. \tag{13}$$

We subsequently define the reduced gravity, $g' = g(\rho_2-\rho_1)/\rho_2$. These equations then tie together with the height equations, which are the shallow-water manifestation of the conservation of mass, to make a complete set

$$\frac{D_1 h_1}{Dt} + h_1\vec{\nabla}\cdot\vec{u_1} = -\frac{h_1 - H_1}{\tau_1} \tag{14}$$

$$\frac{D_2 h_2}{Dt} + h_2\vec{\nabla}\cdot\vec{u_2} = -\frac{h_2 - H_2}{\tau_2} \tag{15}$$

$$h_1 + h_2 = H_1 + H_2 = H_{tot}, \tag{16}$$

where we have included on the RHS of equations (14)-(15) some dissipative terms representing Newtonian cooling towards the equilibrium heights for the two layers on timescales of τ_1 and τ_2. Damping on height in the shallow-water equations is equivalent to damping temperature in the full equations, as can be seen by comparing the model's thermal-wind equation to that in the primitive equations.

The choice to relax back towards the constant equilibrium height, rather than one that varies with latitude (as might be expected for an Earth-like shallow-water model) is made to represent the radiative-convective equilibrium state at the bottom of the weather layer on Jupiter. There the dominant heat source is the internal heat flux, which is often taken to be constant in space. Any influence from short-wave incoming radiation from the sun is likely to be small at such a depth, meaning that latitudinal gradients in the equilibrium heights ought to be minimal. There is some evidence to suggest, however, that the heat flux may not in fact be uniform, but may peak in the polar regions Pirraglia (1984), suggesting other equilibrium heights might be appropriate. For simplicity, however, we choose to consider a constant equilibrium height, with alternative choices providing an interesting avenue for future work.

Equations (12) - (16) represent a complete set, having 7 equations and 7 unknowns. The unknowns are u_1, v_1, u_2, v_2,

h_1, h_2 and $\mathcal{P}$.

2.2 | Approximating the 2-layer model for 1.5 layers

In a 1.5-layer model the lower layer has a fixed velocity field, owing to the assumed large mass of the deeper lower layer. In the ocean-like setup of such a model, we would take $\vec{u_2} = 0$, and use (13) to find that

$$\frac{1}{\rho_2}\vec{\nabla}\mathcal{P}(\lambda,\phi,t) = -g'\vec{\nabla}\eta, \tag{17}$$

which would allow us to rewrite equation (12) as

$$\frac{D_1\vec{u_1}}{Dt} + \vec{f}\times\vec{u_1} = g'\frac{\rho_2}{\rho_1}\vec{\nabla}\eta. \tag{18}$$

If we make the Boussinesq approximation that $\rho_2/\rho_1 \approx 1$, and note that $h_1 = H_1 - \eta$ we can recover equation (3.41) in Vallis (2017) for a 1.5-layer ocean model,

$$\frac{D_1\vec{u_1}}{Dt} + \vec{f}\times\vec{u_1} = -g'\vec{\nabla}h_1. \tag{19}$$

But in the Jupiter context, we want something different. We want to specify $\vec{u_2} = (u_{20}(\phi), 0)$, i.e. a statistically-steady purely zonal flow. To see the consequences of this, we substitute this profile into equation (13). In that case, the advection term is identically zero, leaving

$$\vec{f}\times\vec{u_2} = -\frac{1}{\rho_2}\vec{\nabla}\mathcal{P}(\lambda,\phi,t) - \frac{g(\rho_2-\rho_1)}{\rho_2}\vec{\nabla}\eta. \tag{20}$$

Because $\vec{u_2}$ is known, we can rearrange for the unknown pressure at the rigid lid, $\mathcal{P}$, and substitute this into the upper-layer momentum equation, giving

$$\frac{D_1\vec{u_1}}{Dt} + \vec{f}\times\vec{u_1} = \vec{f}\times\vec{u_2} + g'\vec{\nabla}\eta, \tag{21}$$

where we have also included the Boussinesq assumption that $\rho_2/\rho_1 \approx 1$. The result is now the momentum equation for the upper layer in the presence of a statistically-steady, purely-zonal flow in the bottom layer.

An interesting limit of these equations can be seen if we assume that the flow in the upper layer is close to geostrophic balance, giving the 1.5-layer model's equivalent of the thermal-wind equation

$$\vec{f}\times(\vec{u_1} - \vec{u_2}) \approx g'\vec{\nabla}\eta, \tag{22}$$

with the interface displacement η playing the role of temperature.

These 1.5-layer equations in equation (21) are completed by the addition of the height equations

$$\frac{D_1 h_1}{Dt} + h_1 \vec{\nabla} \cdot \vec{u_1} = -\frac{h_1 - H_1}{\tau_1} \tag{23}$$

$$\frac{D_2 h_2}{Dt} = 0, \tag{24}$$

$$h_1 + h_2 = H_{tot} \tag{25}$$

which are the same as equations (14)-(16), except that now the $h_2 \vec{\nabla} \cdot \vec{u_2}$ term is zero, given that the deep zonal flow is zonally-symmetric. We have additionally taken the radiative cooling time of the lower layer $\tau_2 \to \infty$, as is justified by its very large mass, meaning the radiative cooling time will be extremely long.

It is interesting to note that although the lower-layer's velocity field is constant in time, this does not mean that the lower-layer's height field is constant in time. This is because, following equation (20), it is possible for the lower layer to maintain its velocity of $u_2 \neq 0$ even when $\vec{\nabla} h_2 = 0$ because $\mathcal{P}$ is present to preserve the balance in equation (20). Therefore η is free to evolve with the upper flow, and the presence of the rigid lid is able to guarantee that u_2 stays constant. It is also important to note that $h_1 + h_2 = H_1 + H_2$ at all times and in all locations. This is yet further proof that h_2 must evolve with time, as if it did not, the constant total depth of the two layers could not be maintained with a non-constant η.

2.3 | Numerical formulation of the 1.5 layer model

We use the shallow-water model developed at GFDL (Geophysical Fluid Dynamics Laboratory), and now packaged as part of the Isca modeling framework (Vallis et al., 2018). This model solves the equations in their vorticity-divergence form using spectral decomposition. The original model is designed for 1-layer shallow water with flat topography, so we have modified the code to allow it to do 1.5-layer dynamics.

To reformulate the 1.5-layer equations described previously in vorticity and divergence, we first form the vorticity equations for the two layers by taking the curl of equation (21) for the upper layer, and the curl of equation (20) for the lower layer. This results in two equations for the vertical components of the vorticity in the two layers

$$\frac{D_1(\zeta_1 + f)}{Dt} + (\zeta_1 + f)\vec{\nabla} \cdot \vec{u_1} = \vec{F} \tag{26}$$

$$f\vec{\nabla} \cdot \vec{u_2} + v_2 \frac{\partial f}{\partial \phi} = 0, \tag{27}$$

where $\zeta_1 = (1/a\cos\phi)\partial v_1/\partial\lambda - (1/a)\partial u_1/\partial\phi$ and $\zeta_2 = (1/a\cos\phi)\partial v_2/\partial\lambda - (1/a)\partial u_2/\partial\phi$. We have also included a forcing on the upper-layer vorticity, $\vec{F}$, which we will use in many of the numerical simulations detailed in subsequent sections. The exact form of the forcing will be discussed in section 2.4. Equation (27) is trivially satisfied when we specify the velocity profile $\vec{u_2} = (u_{20}(\phi), 0)$. To get the remaining two momentum equations, we form the divergence equation for each layer.

$$\frac{\partial(\vec{\nabla} \cdot \vec{u_1})}{\partial t} + \vec{\nabla} \cdot \vec{A_1} + \frac{1}{2}\nabla^2(|\vec{u_1}|^2) = -\frac{1}{\rho_1}\nabla^2\mathcal{P} \tag{28}$$

$$\frac{1}{a}\frac{\partial}{\partial\phi}(u_{20}(\phi)f(\phi)) = -\frac{1}{\rho_2}\nabla^2\mathcal{P} - g'\nabla^2\eta, \tag{29}$$

where $\vec{A}_1 = (\zeta_1 + f)\vec{k} \times \vec{u}_1$, where $\vec{k} = (0, 0, 1)$ is the unit vector in the vertical direction, and a is the planetary radius. As previously, the lower level equation can be rearranged for $\mathcal{P}$, which can then be substituted into the upper-layer equation to give

$$\frac{\partial(\vec{\nabla} \cdot \vec{u}_1)}{\partial t} + \vec{\nabla} \cdot \vec{A}_1 + \frac{1}{2}\nabla^2(|\vec{u}_1|^2) = \frac{1}{a}\frac{\partial}{\partial \phi}(u_{20}(\phi)f(\phi)) + g'\nabla^2\eta, \tag{30}$$

where we have again used the Boussinesq approximation that $\rho_2/\rho_1 \approx 1$. A complete set is then formed by combining equations (26)- (29) with the height equations (23)-(25). It is noted that the numerical implementation of the model deals with all the height equations scaled by g'. In this formulation we do not have to choose specific values for g', H_1, or ρ_2, but only for the product $g'H_1$, the value of which determines the L_D values used in the simulations to follow.

2.4 | Forcing

In the experiments described below, forcing is applied to the 1.5-layer system that represents small-scale stirring on Jupiter. The forcing is similar in formulation to that in Vallis et al. (2004) and Scott and Polvani (2007). It is random in space, with a narrow range of wavenumbers forced. It is Markovian in time, with a decorrelation time of 10 planetary rotations, as in Scott and Polvani (2007). The realism of such a forcing for Jupiter is debated. It is sometimes taken to represent the effects of moist convection, but observational evidence suggests that the patterns of Jovian moist convection are spatially inhomogeneous, with observed lightning confined to the cyclonic belts Porco et al. (2003), with a significant amount of lightning recently observed near the north pole (Brown et al., 2018). These polar observations further suggest that Jupiter's internal heat may well be escaping predominantly in the polar regions, as discussed in Pirraglia (1984). This would suggest that a fruitful way of forcing such a system would be to use spatially inhomogeneous forcing confined to cyclonic regions, as was done in Thomson and McIntyre (2016). However, in this paper we choose instead to focus on the simpler case of forcing over the entire domain. This may loose some 'realism' compared to the real planet, but is a simpler first approach, and connects more easily to other shallow-water turbulence studies, e.g. Scott and Polvani (2007).

An alternative motivation for such a forcing is that it is representative of baroclinic instability, which is perhaps consistent with the turbulent structure functions derived from Jupiter observations in Young and Read (2017), which show a spectral divergence of energy around the deformation scale. This suggestion would promote a more spatially-homogeneous forcing, and is an additional reason for our choice of this in the present work.

The forcing we use is confined to a small range of wavenumbers, where the total wavenumber is placed between two limits. The work of Young and Read (2017) suggests that this range should be close to the L_D value chosen for a particular experiment. For simplicity, however, we choose our wavenumber range to be as small as possible for the horizontal resolution of the simulation carried out. Specifically, runs at T170 are forced in a wavenumber range between 79 and 85. This wavenumber choice corresponds to a spatial scale of $\sim 0.074a$, and so is small enough to be smaller than the polar L_D value in any of the T170 simulations shown in this paper, but also large enough so that it is well clear of the small-scale hyperdiffusion that is included for numerical stability. The same approach is taken for our T341 simulations, which are forced in a wavenumber range between 164 and 170. This corresponds to a spatial scale of $\sim 0.037a$, which is close to L_D in the T341 simulations shown in this paper, and so is more similar to the regime described in Young and Read (2017). An interesting avenue of further work with this model would be to look at the impact of forcing scale on the coupling and energy cascades, but here we focus purely on the vertical coupling, and keep the forcing wavenumber constant for a given resolution.

3 | A SCALING ANALYSIS TO PREDICT THE COUPLING MAGNITUDE

In order to guide our computational work, we begin by considering ways in which the deep flow could influence the weather-layer. We consider two of those here, and then derive a simple scaling for how the magnitude of these mechanisms might vary with our parameters.

The first coupling mechanism to be considered is radiative damping. Considering the thermal-wind equation in (22), it is clear that the shear between the two layers is related to the slope of the interface, η. Because radiative damping of the type in equation (23) relaxes η back towards zero, radiative damping is a mechanism for removing spatial contrast in η and therefore removing vertical shear between the layers. One factor determining the efficiency of this coupling mechanism is the relative strengths of the radiative damping, τ_1 and the forcing. With radiative damping much stronger than the forcing, the system will relax back towards η being zero, and as such will have no vertical shear. Whereas with stronger forcing the system should have non-zero η, and therefore have vertical shear.

The second coupling mechanism to be considered is the effect the deep jets have on η, and how this affects the dynamics of the upper-layer flow. To see this, consider the PV in the upper layer, which can be found by combining equation (21) with (23) to get

$$\frac{D_1 Q_1}{Dt} = \frac{Q_1}{h_1}\left(\frac{h_1 - H_1}{\tau_1}\right), \tag{31}$$

where

$$Q_1 = \frac{(\zeta_1 + f)}{h_1}. \tag{32}$$

The PV equation encompasses all of the relevant dynamics for the upper layer. If we discount the radiative damping, then the only dependence on the lower layer in equation (31) is via the η in $h_1 = H_1 - \eta$ in equation (32). However, if $\eta \ll H_1$ then clearly $Q_1 \approx (\zeta_1 + f)/H_1$, and the upper layer will not know about the deep layer at all. But if η is of the same order as H_1, or close to it, then the PV will know about the layer depth, and thus the deep jets.

How the size of η/H_1 relates to the vertical coupling of the jets is more subtle than this first argument might suggest. One way of making η/H_1 very small is for the vertical wind-shear to be zero, i.e. a strong vertical coupling between the two layers, as in equation (22). However, the multiplicative g' in the thermal wind relation means that a given amount of vertical wind shear can lead to differing magnitudes of η depending on the size of g'.

To see this, we perform a dimensional analysis of the approximate thermal-wind equation (22), giving

$$\eta \propto \frac{f \Delta U a \Delta\phi}{g'}, \tag{33}$$

where f is the Coriolis parameter, ΔU represents the velocity differences between the layers, and $\Delta\phi$ represents the latitudinal scale of the deep jets. So for a given planet, where f, a and $\Delta\phi$ are known, a given amount of vertical wind shear will have differing effects on the magnitude of η depending on the value of g'.

To understand the important quantity for the impact of η on the upper-layer PV, we consider the ratio η/H_1. We can write H_1 in terms of the Rossby-deformation scale, L_D as

$$H_1 = \frac{(L_D f)^2}{g'}, \tag{34}$$

meaning that their ratio is proportional to

$$\frac{\eta}{H_1} \propto \frac{\Delta U a \Delta\phi}{f L_D^2} \tag{35}$$

We can also form this in terms of dimensionless quantities, by taking a Rossby number $Ro = U_0/(f a \Delta\phi)$ and a Burger number $Bu = (L_D/a\Delta\phi)^2$, meaning that

$$\frac{\eta}{H_1} \propto RoBu^{-1}. \tag{36}$$

If we increase the value of this ratio, we can make η a larger fraction of H_1, and therefore make Q_1 more sensitive to the shape of the interface. The free parameters in this scaling are the factors controlling L_D, which is again related to g'. So for a given amount of vertical wind shear, the impact of the interface displacement on the upper-layer PV is determined by the size of L_D, with large L_D leading to small η/H_1, and therefore a small impact of the wind-shear on the upper-level flow, and vice versa for small L_D.

It is therefore suggested that having a large L_D will make vertical coupling more difficult, as a large amount of vertical wind shear will still only have a small impact on the upper-layer PV, meaning the upper-layer flow cannot effectively feel the impact of the deep flow's presence / structure. A small L_D, however, will mean a given vertical wind shear will have a larger impact on the upper-layer, meaning that small L_D systems are expected to stand a better chance of achieving a strongly-coupled state.

It is to be noted, however, that $L_D = \sqrt{g' H_1}/f$ varies with latitude, as a result of the factor of f in the denominator. This means that the strength of radiative damping, and of coupling, will likely depend on latitude. As a further note, when values of L_D are quoted in subsequent sections, this value refers to the value of L_D at the pole, i.e. $L_D(\phi = \pi/2) = \sqrt{g' H_1}/2\Omega$, from which the values at other latitudes can be deduced.

It is not entirely clear, of course, exactly what impact the upper jets feeling the interface displacement from the lower jets will have on the inter-layer coupling when other factors are accounted for, such as forcing and instabilities. Indeed, radiative damping is proportional to gradients in η, meaning that small L_D, corresponding to large η, will also mean that radiative damping is likely to be stronger than for large L_D. The combination of these effects leads to the prediction that small L_D will lead to significant inter-layer coupling. Given these complications this investigation is continued with the numerical model in section 4

4 | RESULTS OF NUMERICAL EXPERIMENTS

4.1 | The role of radiative damping

To verify the idea that, without any forcing, the effect of radiative damping is to make the weather-layer jets match the deep jets, we run numerical experiments of this type. We begin by prescribing the deep jets to have the profile $\overline{u}_2 = (50\cos(n\phi), 0)$, where n is the meridional wavenumber. When varying n, we find that the radiative damping is strongest when the spacing is large, i.e. n is small. This can be seen by comparing the coupling after 360 Earth days in figure 2. In the midlatitudes, the profile of $\overline{u}$, representing the zonal-mean of the zonal wind, after 360 days closely matches the case with large deep-jet spacing, but does not yet closely match in the cases with small deep-jet spacing. This is consistent with the scaling estimates in (36), which suggested η, and thereby radiative damping, would be largest for large $\Delta\phi$. Near the equator, however, radiative damping alone seems unable to mediate a coupling between the deep and weather-layer jets. This is a manifestation of previous work, e.g. Haynes (1998) and discussion in Scott and

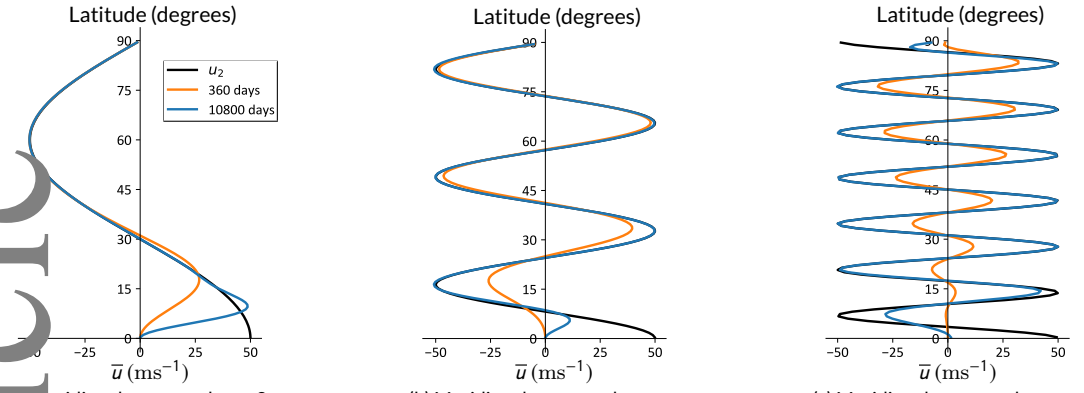

(a) Meridional wavenumber = 3 (b) Meridional wavenumber = 11 (c) Meridional wavenumber = 26

FIGURE 2 The three panels show zonal-mean zonal-wind profiles with various deep meridional wavenumbers in [illegible] with $\tau = 100$ Jovian days and $L_D = 0.1a$. The coloured lines represent the upper-layer flow at two different times (legend in figure 2a, with times in Earth days) and the black line represents the deep flow, u_2. As can be seen, with a low [illegible]dional wavenumber of 3, the upper layer evolves to match the deep jet profile within one Earth year, apart from at the equator. For higher wavenumbers the equilibration takes longer, but is still happening, with the ubiquitous exception of the equatorial regions. Note that we only show the northern-hemisphere of our global runs, as there is nor[illegible]n-south symmetry.

[illegible]ani (2007), who argue that radiative damping places very little constraint on angular momentum in the tropics. In our [illegible]ystem, this is because the impact of the jets on the height field is weak in the tropics, meaning that damping out η variations is not effective at changing the vertical shear. As such, radiative damping alone can be seen as a coupling me[illegible]anism, but only outside the tropics.

We now consider a set of forced simulations with radiative damping. We show the results of this experiment in [illegible]gure 3. The forcing is between wavenumbers 79 and 85, and is Markovian in time with a decay time of 10 Jovian days. [illegible]e horizontal resolution of these calculations is T170. In these experiments we change the strength of the radiative damping, and find that, consistent with our predictions, strong radiative damping is sufficient to suppress any effects of the forcing, as seen in panel 3a, apart from in the tropics where radiative damping is ineffective. As the radiative damping is w[illegible]eakened, the latitudinal region near the equator where the forcing is effective gradually expands polewards, until th[illegible]whole planet is able to decouple its upper jets from its deep jets without radiative damping in panel 3d. It is to be noted that these experiments were conducted with $L_D = 0.1a$, for which the ratio η/H_1 is small, meaning other coupling me[illegible]anisms are weak.

4.[illegible] | The role of L_D in setting the effectiveness of radiative damping

[illegible]aving seen the role that the strength of radiative damping plays in setting the coupling of the two layers, it is important to consider how other parameters of the model may affect the radiative damping. To see this, consider the height ev[illegible]ution equation (23). If we re-write this in terms of η we have

$$\frac{D\eta}{Dt} = h_1 \vec{\nabla} \cdot \vec{u_1} - \frac{\eta}{\tau_1}. \tag{37}$$

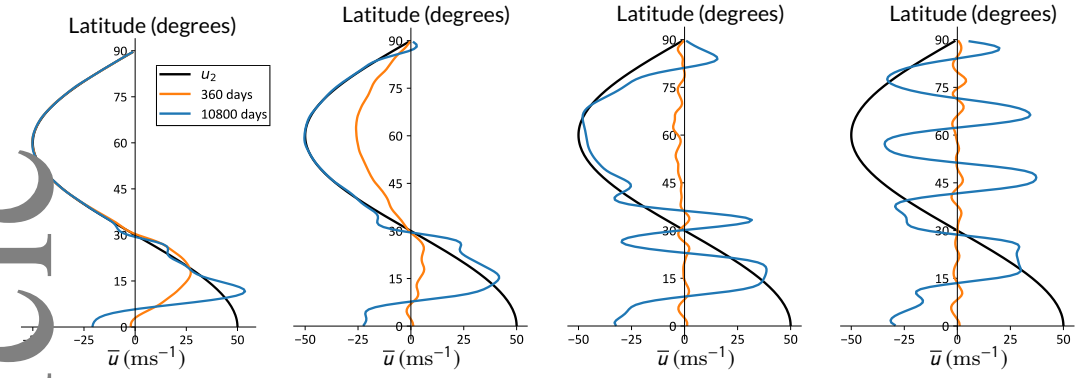

(a) Damping time = 100 rotations (b) Damping time = 1000 rotations (c) Damping time = 10000 rotations (d) No radiative damping

FIGURE 3 Zonal-mean zonal-wind profiles in runs with common forcing and $L_D = 0.1a$ with different values of τ. The colours correspond to the times shown in the legend of panel 3a.

If the horizontal divergence of the flow is zero, say if e.g. $\vec{u_1} = (U_0 \cos(n\phi), 0)$, then we have

$$\frac{\partial \eta}{\partial t} = -\frac{\eta}{\tau_1}, \tag{38}$$

meaning η will decay exponentially towards zero on a timescale of τ_1. However, clearly the horizontal divergence of the flow will not always be zero, and so it is important to consider what happens in this case. To test this, we perform a series of unforced simulations with a single τ_1 and deep jets with $u_2 = 50 \cos 27\phi ms^{-1}$, and vary the deformation scale in a range from $L_D = 10a$ to $L_D = 0.025a$. In these experiments the upper jets start at rest and evolve to match the deep jets outside of the tropics via an exponential decay. We can fit a timescale τ_{decay} to this decay using

$$|u_1(\phi) - u_2(\phi)| = 50 \cos(27\phi) e^{-t/\tau_{\mathrm{decay}}(\phi)} \tag{39}$$

Figure 4a plots the measured $\tau_{\mathrm{decay}}(\phi = 66.67°)$ in units of τ_1 against L_D^2, where $\phi = 66.67°$ is chosen because it is the peak of one of the deep jets. As is clear, τ_{decay} is significantly larger than τ_1 for large L_D, with τ_{decay} only approaching τ_1 at very small L_D. This confirms that L_D has a significant impact on the efficiency of radiative damping, with large L_D making radiative damping much weaker for a given τ_1.

The scaling of τ_1 with L_D^2 is related to the size of the $h_1 \vec{\nabla} \cdot \vec{u_1}$ term in equation (37). This term gets significantly larger for large L_D, which explains the clear departure from the simple exponential decay of equation (38). The h_1 part of the $h_1 \vec{\nabla} \cdot \vec{u_1}$ term implies a scaling with L_D^2, which is reflected in figure 4a.

It is also noted that the size of the measured τ_1 is a function of latitude, with the timescale being shortest at the pole, and longest near the equator. The variation with latitude is also explained by the size of the $h_1 \vec{\nabla} \cdot \vec{u_1}$ term in equation (37) with its implication that $\tau_1 \propto h_1 \propto L_D^2$. This implies that τ_1 will scale with $1/f^2$, or $1/\sin\phi^2$. The proportionality between τ_1 and $1 \sin\phi^2$ is shown in figure 4b, with τ_{decay} on the y axis having been scaled by $1/L_D^2(\phi = 90°)$ in order to remove the dependence on the polar L_D found in figure 4a, allowing the latitudinal dependence of the decay with multiple L_D values to be compared on one plot.

This analysis confirms that it is not enough to simply identify the timescale of radiative damping τ_1, but also the local value of L_D, in order to determine how effective radiative damping will be.

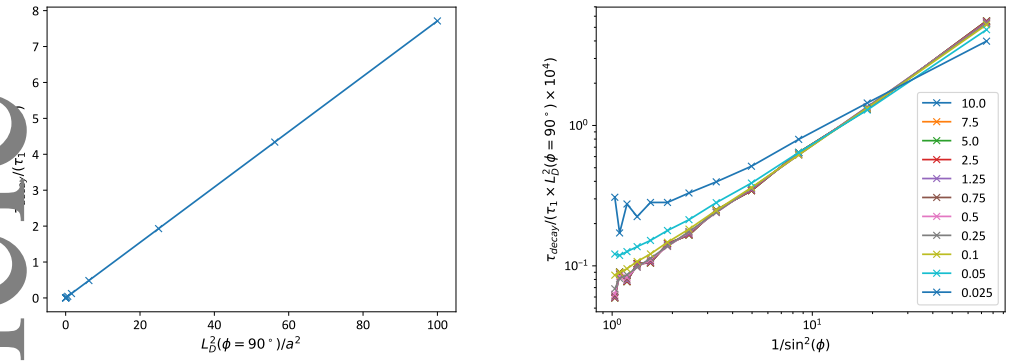

(a) τ_{decay} as a function of L_D^2

(b) τ_{decay} plotted against $1/\sin^2(\phi)$. Colours denote different values of L_D in units of the planet radius, a.

FIGURE 4 Panel 4a shows the decay constant from equation (39) for runs with various values of L_D. Panel 4b shows how this decay time varies with latitude.

4.3 | The role of L_D in the absence of radiative damping

To assess the role of L_D in the coupling of the weather-layer jets to the deep jets in the absence of other effects, we conduct the experiments in this section without any radiative damping. Because there is no form of dissipation, the system does not reach a steady state, and so we examine conditions after 10,800 Earth days. We choose a deep-jet wavenumber of $n = 26$, and a specified amplitude and wavenumber of forcing across all experiments.

Profiles of northern-hemisphere zonal-mean zonal wind are shown in figure 5. As predicted by the scaling of section 3, large L_D leads to weather-layer jets that are decoupled from those in the deep layer at all latitudes. As we decrease L_D, the jets start to become coupled at high latitudes, and are more prone to departures at low latitudes. This is likely because of L_D being smallest at high latitudes, leading to more significant impact of η on Q_1 there, and so encouraging tighter coupling.

At $L_D = 0.01a$, we find strong coupling between the deep and shallow jets at low latitudes, and a suppression of jet structures at high latitudes, which is the opposite of that found in the case with $L_D = 0.05a$. This is very similar to the results found without deep jets by Scott and Polvani (2007), who found a similar suppression of jets at high latitudes when using small L_D. This idea was discussed at length by Theiss (2004), who relate the suppression to the well-known Rhines length, written below as a Rhines wavenumber, n_{Rh}, following Scott and Polvani (2007).

$$n_{Rh} \sim \sqrt{\left(\frac{a\Omega}{U}(1-\alpha)\right)} \tag{40}$$

$$\alpha = \frac{aU}{\Omega L_D^2} \tag{41}$$

In typical studies of jet formation $L_D \to \infty$, and so $\alpha \to 0$, meaning that we recover the familiar $n_{Rh} \sim \sqrt{a\Omega/U}$, where U is a typical velocity scale (For clarity, we will always take $U = U_{RMS}$). However, when L_D is finite and small, $\alpha > 1$, meaning that n_{Rh} is undefined, and jets are unable to form. As discussed previously, L_D is smallest at the pole, meaning that α can be thought of as being largest at the pole, and so the high-latitude jets are the first to be disrupted with small L_D.

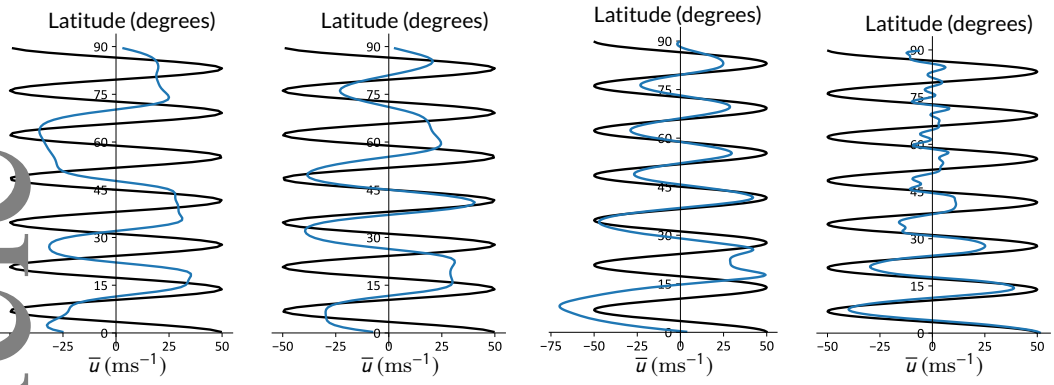

(a) $L_{Dp} = 10a$; T170 (b) $L_{Dp} = 0.1a$; T170 (c) $L_{Dp} = 0.05a$; T341 (d) $L_{Dp} = 0.01a$; T341

FIGURE 5 The differing responses of the upper jets to deep jets with $n = 26$ with different values of L_D. The horizontal resolution of each run is also noted, as very small L_D requires higher resolution to resolve the eddy scale. The colours correspond to those in the legend of figure 3a.

It is interesting that this argument still applies when deep jets are present, as it implies that the upper layer flow is still forming jets via turbulent cascades, rather than a simple relaxational process via e.g. the system trying to minimise its own potential energy. This means that, without radiative damping or another coupling process, it is difficult for the jets to be coupled at high latitudes at small L_D. When α is everywhere less than 1, however, the high-latitude jets are better coupled than those at low latitudes. Clearly, therefore, L_D plays a significant role in determining the coupling.

An additional question is whether or not the deep jets make any difference to the flow at high latitudes when $L_D = 0.01a$ despite the jets not matching. To answer this question, figure 6 shows the vorticity fields in experiments with $L_D = 0.01a$, with figure 6a having no deep jets, and figure 6b being the case with deep jets from figure 5d. As in Scott and Polvani (2007), the case with no deep jets has chaotic polar regions, being dominated by large-scale vortices rather than jet streams. In the case with deep jets, however, the vorticity field is much more zonal at high latitudes, even though the resulting zonal flows are very weak. This suggests that the presence of the deep jets is helping to change the character of the weather-layer flow, even if the jet-velocities are not coupled.

It might be argued that the real Jupiter is somewhere between these two extremes, with recent Juno observations revealing polar regions with significant vortices present, much like in figure 6a, but also including highly-organised vortex crystals centred on the pole (Adriani et al., 2018; Tabataba-Vakili et al., 2020), with the symmetry more reminiscent of those in figure 6. Neither of the model configurations in figure 6 show such crystalline vortex structures, but it remains a possibility that some of the symmetry in Jupiter's polar regions has a deep origin, much like in figure 6b, with a possible moist-convective origin for the regions cyclones O'Neill et al. (2015). Further work will therefore be undertaken to investigate any potential role for deep jets in symmetrising the polar regions on Jupiter.

4.4 | The role of deep-jet spacing

In experiments without deep jets, the number of upper-layer jets that form in our experiments is well-described by the n_{Rh} of equation (40). One of the contributing factors in this equation is the value of U_{RMS}, with large U_{RMS} leading to a small wavenumber, and therefore relatively few jets, and vice versa. In systems such as the one presented here, U_{RMS} is determined by a balance between the energy input rate, ϵ, and the damping rate.

In this section, in order to isolate coupling mechanisms, we proceed without any radiative damping. This means that

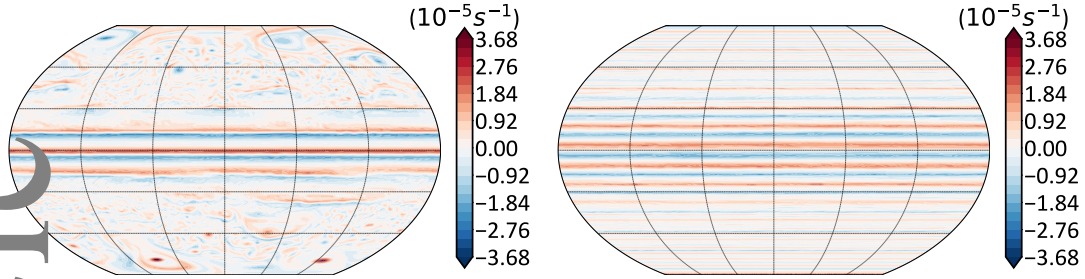

(a) No deep jets

(b) Deep jets with $50ms^{-1}$ magnitude and $n = 26$.

FIGURE 6 The relative vorticity field is shown at $t = 10,800$ Earth days in cases with and without deep jets.

the total energy increases throughout the simulation, and hence U_{RMS} increases with time, meaning that n_{Rh} decreases with time. This time variation is useful for studying under what circumstances the upper jets are most coupled to the deep jets. We perform a series of experiments with $L_D = 0.05a$, meaning $\alpha < 1$, the same forcing as in the previous section and deep jets with the form $\vec{u}_2 = (50\cos(n\phi), 0)$, where n is varied between 3 and 79. To assess the coupling between the upper jets and the deep jets, we calculate the correlation coefficient between the zonal-mean zonal wind in the upper layer with the zonal-wind deep-jet profile. The correlation coefficient measures both whether the jet spacing is similar in the two layers, but also if the phase of the jets are similar. I.e. two profiles with the same spacing but different 'phases', e.g. $u_1 = 20\sin(n\phi)$ and $u_2 = 20\cos(n\phi)$ have the same spacing, but would have a correlation coefficient of zero, as they are completely out of phase.

To assess the coupling between the deep jets and the upper jets we show three different correlation coefficients as a function of deep jet wavenumber in figure 7a. The blue line shows the correlation coefficient between the upper jets and the deep jets after 10,800 days of simulation with a variety of deep jet wavenumbers. It is clear that the upper jets are most correlated with the deep jets with a deep-jet wavenumber of 23, with 21 also displaying a high correlation coefficient, with larger and smaller deep-jet wavenumbers displaying significantly lower correlations. Because all the experiments have the same forcing, and hence the same energy injection rate, the U_{RMS} values are similar across the experiments. At $t = 10,800$ days, the U_{RMS} value corresponds to an $n_{Rh} = 22.43$ when averaged across all the experiments, which is shown by the vertical red line in figure 7a. That the correlation coefficient is highest when the upper-jet wavenumber, n_{Rh}, is closest to the wavenumber of the deep jets n, is perhaps unsurprising at first sight. However the correlation coefficient is sensitive both to the spacing and the phase of the jets. This therefore implies non-trivial coupling, with the upper-jets matching the phase and spacing of the deep jets when n_{Rh} is close to the deep jet wavenumber.

This result is further illustrated by figure 8, which shows four of the cases from figure 7a, with the case with $n = 19$ showing the upper jets matching the deep jets in both spacing and latitudinal phase.

To further illustrate the phases locking, figure 7a also plots the correlation coefficients between the upper jets at $t = 10,800$ days and an artificial deep jet profile. This artificial profile is created offline, and has its latitudinal phases shifted by $n\pi/2$ compared with the phases of the deep jets used in the simulations. For the jets with very low deep-jet wavenumber, the correlation with these shifted deep jets is almost as much as with the original deep jets, confirming that the latitudinal phases are not coupled in these cases. However, for the cases where significant coupling does take place, the correlation is much higher with the real deep jets than the shifted deep jets, confirming this coupling of the phases as being non-trivial.

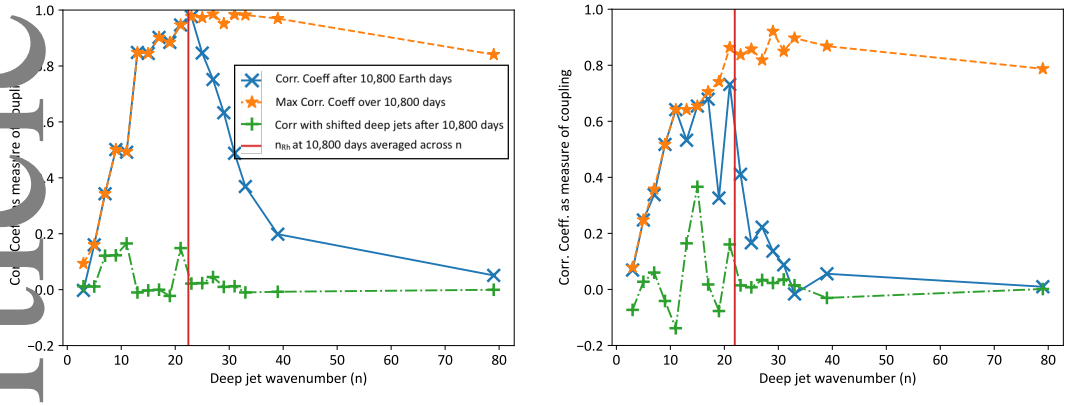

(a) $L_D = 0.05a$ (b) $L_D = 0.1a$

FIGURE 7 Correlation coefficients are shown between the deep jet profiles and those in the upper layer when n is varied. The left-hand panel is for $L_D = 0.05a$, and the right-hand panel is for $L_D = 0.1a$.

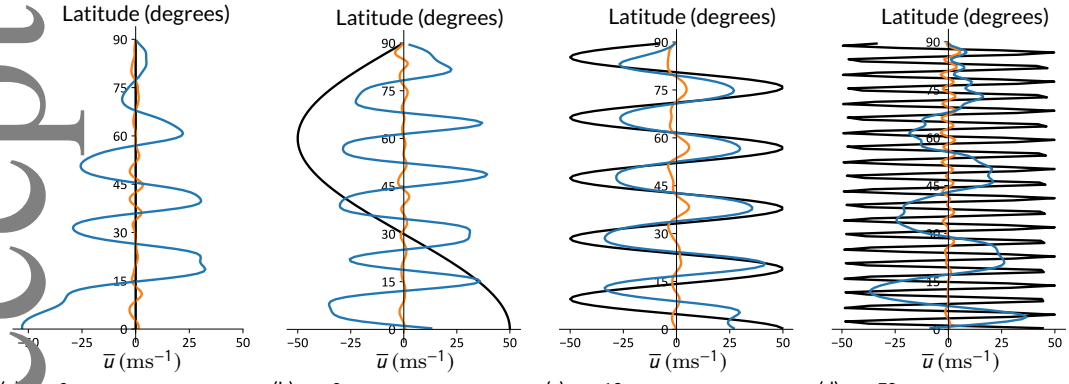

(a) $n = 0$ (b) $n = 3$ (c) $n = 19$ (d) $n = 79$

FIGURE 8 The response of the upper jets is shown to a change in deep meridional wavenumber (n) at a constant $L_D = 0.05a$. The colours correspond to the legend in figure 3a.

The aforementioned time-variation of n_{Rh} also allows us to check our idea that the coupling is strong in phase and spacing when n_{Rh} approaches n. The orange line in figure 7a shows the maximum correlation coefficient achieved over the previous 10,800 days of simulation. The maximum correlation achieved in the cases with $n > n_{Rh}$ is higher than the correlation at $t = 10,800$, suggesting that, at earlier times when n_{Rh} was larger, significant coupling between the jet streams was found, but that this coupling was not strong enough to stop the upper-jet streams from continually decreasing n_{Rh} and moving to a non-coupled state.

The mechanism for why jets with $n_{Rh} \sim n$ have their phases locked with the deep jets is not made clear by these experiments. One possible explanation is that, by matching the phases, the interface displacement η is minimized, and so the potential energy of the system is minimized. Further work is required, however, to identify this mechanism.

As an additional check on the story described above, we also ran the same set of experiments with $L_D = 0.1a$, with the correlation coefficients plotted in figure 7b. This figure tells a similar store to figure 7a, with correlation coefficients at $t = 10,800$ days being highest near the n_{Rh} value at $t = 10,800$ days, and correlation coefficients at $t = 10,800$ days with $n > n_{Rh}$ being lower than correlation coefficients at earlier times (i.e. the orange line lies significantly above the blue line in the region $n > n_{Rh}$). However, there is more complexity in the region $n < n_{Rh}$ for $L_D = 0.1a$ than there was for $L_D = 0.05a$, specifically that some cases, e.g. $n = 19$ have lower correlations at $t = 10,800$ days than at earlier times, meaning that their correlations were higher at earlier times when n_{Rh} was further from n. The reason for this is almost certainly that the coupling is weaker with a larger L_D, also signified by the fact that the highest correlations with $L_D = 0.1a$ are lower than with $L_D = 0.05a$. This means that the upper jets are much less aware of the deep jets, and so less likely to couple strongly, especially when n is not close to n_{Rh}. This is also demonstrated by the fact that correlations with the artificially-shifted deep jets (green line) are higher for $L_D = 0.1a$ than for $L_D = 0.05a$, suggesting more of the correlation for $L_D = 0.1a$ comes about randomly than in $L_D = 0.05a$.

The present section affirms the results of section 4.3, namely that the value of L_D plays a key role in the coupling of the upper jets to the deep jets, but small L_D is not sufficient for coupling to take place, and must be accompanied by a deep jet wavenumber that is somewhat close to the upper-jet spacing that would be found from a balance between ϵ and the appropriate damping timescale.

5 | A REALISTIC BALANCE OF COMPETING EFFECTS

In the previous sections we have shown the dependence of inter-layer coupling on important parameters of the system. The coupling is particularly dependent on L_D, the deep-jet spacing, and the factors that combine to determine n_{Rh}, being the energy-injection rate and the damping strength. In this section we look at our most Jupiter-like setup to try to ascertain what the balance of effects may be in reality.

Observational estimates of L_D come mostly from a variety of sources. In order of increasing values, Thomson and McIntyre (2016) showed their quasi-geostrophic model showed the most realistic behaviour with $L_D = 0.017a$, Read et al. (2006) used an assumption of marginality with respect to Arnol'd's second stability criterion to estimate a likely range of between $0.021a$ and $0.029a$ (see their figure 13). Two studies using models of Jupiter's large southern-hemisphere vortices to find likely values for L_D were Cho et al. (2001) and Shetty and Marcus (2010), who give likely values of $0.029a$ and $0.027a$, respectively. The largest estimate comes from measurements of the waves emanating from the impact of the comet Shoemaker-Levy 9 by Hammel et al. (1995), with a value of $0.032a$, although some doubt has been cast as to the validity of this approach by Walterscheid (2000).

Given this range of estimates, we choose an intermediate value of $L_D = 0.025a$ following Scott and Polvani (2007). We are unable to study values of L_D much lower than this as, consistent with the scaling of equation (36), η becomes a

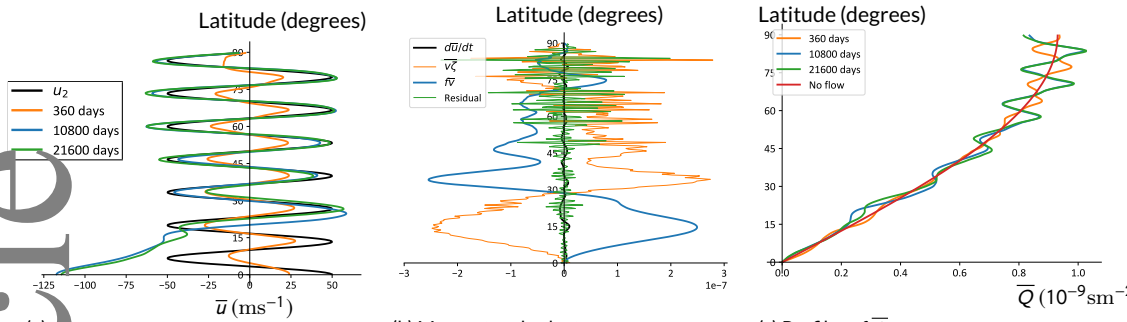

(a) $\overline{u}$ (b) Momentum budget (c) Profiles of $\overline{Q}$

FIGURE 9 The first panel shows the zonal-mean zonal-wind averaged over the final 30 days of a 21,600 day runs. The ϵ value for this case is $\sim 0.75 \times 10^{-5} m^2 s^{-3}$, $\tau_1 = 10,000$ Jovian days. The second shows the momentum budget for this case, and the third shows profiles of the zonal-mean potential vorticity at different times for this same case.

large fraction of H_1, such that shallow-water is no longer an appropriate model.

In terms of Jupiter's energy-injection rate, which we use as a proxy for our forcing strength, one of the most comprehensive estimate comes from the fitting of an $n^{-5/3}$ model to the residual energy spectrum derived from Jupiter's cloud-tracked winds in Galperin et al. (2014). This value is $\epsilon \sim 0.5 - 1 \times 10^{-5} m^2 s^{-3}$, depending on the cloud-tracking data used. More recent work by Young and Read (2017) has, however, updated this estimate using third-order structure functions derived from Cassini data, and find the input power to be $\sim 1 \times 10^{-4} m^2 s^{-3}$, which is significantly higher than the previous estimate. There are significant complications with applying both estimates globally, including that the latter assumes homogenous isotropic turbulence, which Jupiter is clearly not on the large-scale (Young and Read, 2017). For simplicity, therefore, we have tuned our forcing amplitude to replicate the smaller value, with the influence of forcing amplitude to be explored further in future work.

In idealised-model studies using white-noise-in-time forcing and simple Rayleigh drag, the energy injection rate, ϵ, and total steady-state energy can be calculated a priori. However, given that we are using Markovian-in-time forcing and a non-Rayleigh-drag dissipation, neither of these quantities can be estimated. We therefore choose to force at small scales (wavenumbers 170-174) in our T341 simulations, and adjust the amplitude of the forcing to get an ϵ value close to $10^{-5} m^2 s^{-3}$.

In terms of radiative damping, an appropriate value is much more difficult to estimate. This is partly due to the complex radiative transfer processes in Jupiter's atmosphere and the unknown conditions beneath the cloud-level, but also because τ_1 represents the integrated effects of radiative damping over the entire weather-layer. To that end, we ran 'realistic' simulations with $\tau_1 = 10,000$ Jovian days, $\tau_1 = 100,000$ Jovian days, and with $\tau_1 = 1,000$ Jovian days, with our order-of-magnitudes being guided by the radiative-damping timescales in figure 177 of Flasar (1989).

For the deep-jet spacing and magnitude, we follow Dowling and Ingersoll (1989) and Thomson and McIntyre (2016) and Kaspi et al. (2018) in choosing a deep-jet spacing that is close to that observed at cloud-level, which we take to be 27. As discussed in section 1, there is significant debate over an appropriate magnitude to choose for Jovian deep jets and so we choose $50 ms^{-1}$ as a compromise between the strong cloud-level jets in low latitudes, and the weaker jets in midlatitudes.

Figure 9 shows a case with our best-guess parameters for realism, with a radiative damping time of 10,000 Jovian days in 9a. In this parameter regime, the midlatitude jets are tightly coupled between the layers, which is a process that is mediated by radiative damping. Comparison with runs with similarly small L_D but no radiative damping in figure 5d suggest that no jets should form at high latitudes in these cases because of the largeness of α. However, this and similar

cases with realistic values suggest that radiative damping is able to overcome this suppression, and form jets at high latitudes despite $\alpha > 1$ there.

The equatorial region, consistent with previous sections, does not feel such a damping, and is robustly retrograde. Weaker retrograde flow is also seen in a similar case with a radiative damping time of 1,000 Jovian days (not shown). There is time-variability in the equatorial flow, however. In both cases the equatorial regions superrotate whilst spinning up until 2,500 Earth days, but then transition to robust subrotation for the remainder of both runs. The stronger subrotation in the case with weaker radiative damping is consistent with this case being more free to decouple its low-latitude jets from the deep jets.

To understand the reasons for this equatorial subrotation, we look at the zonal-mean momentum budget, the equation for which is

$$\frac{\partial \overline{u}}{\partial t} = \overline{v\zeta} + f\overline{v} + \overline{\mathrm{diss}} + \overline{\mathrm{forcing}}, \tag{42}$$

where $\overline{\mathrm{diss}}$ and $\overline{\mathrm{forcing}}$ represent the zonal-mean effects of the dissipation and the forcing. It is to be noted that the $v\zeta$ term involves the full v and ζ fields multiplied together, with $\overline{v\zeta} = \overline{v}\,\overline{\zeta} + \overline{v'\zeta'}$, where primed quantities represent departures from the zonal mean. Under the quasi-geostrophic assumption, $\overline{v} = 0$, meaning that $\overline{v\zeta} = \overline{v'\zeta'}$, but the full shallow water equations used in the present study do not guarantee that $\overline{v} = 0$, meaning the full $\overline{v\zeta}$ must be retained.

The only non-numerical dissipation in this model is radiative damping, so $\overline{\mathrm{diss}}$ represents the momentum damping felt as a result of the damping on the height field. By contrast $\overline{\mathrm{forcing}} \sim 0$, which is ensured by the randomness of the forcing in space, and the short decorrelation timescale in time. The terms in this equation for the case shown in figure 9a are shown in figure 9b. The flow is close to being statistically steady, so $\partial\overline{u}/\partial t$ is close to zero at all latitudes. In equatorial regions, consistent with previous discussion, the dissipation plays little role in the balance, with $\overline{v\zeta} \approx -f\overline{v}$. At higher latitudes, dissipation plays a more significant role, as represented by the residual term in the budget, although both the residual and $\overline{v\zeta}$ are rather noisy, despite being time-averaged for 10 Earth years, making interpretation difficult. In terms of the equatorial subrotation, the view provided by the vorticity fluxes, $\overline{v\zeta}$, or an equivalent view from the momentum fluxes, $\overline{u'v'}$, suggest that positive u is being exported out of the equatorial regions and into high latitudes. This is contrary to the expectation that Rossby waves generated in equatorial regions should leave behind a deficit of negative momentum, leading to equatorial superrotation (see e.g. Vallis, 2017). It is therefore hypothesised that either our forcing is unable to generate sufficient large-scale Rossby waves in equatorial regions to have this mechanism produce equatorial superrotation, or that similar Rossby waves are generated at all latitudes, and break predominantly in equatorial regions thus leading to subrotation. Further work is required to see if a prograde flow could be found for realistic Jovian parameters with alternative forcings.

In terms of the mid-to-high latitudes, one notable feature of the eddy momentum flux, $\overline{u'v'}$ in the case shown in figure 9 with $\tau_1 = 10,000$ Jovian days, and in the case with $\tau_1 = 100,000$ Jovian days (not shown) is that it is uncorrelated with the zonal shear, $d\overline{u}/d\phi$. A correlation between these terms would suggest the passive-shearing of eddies leading to enhancement of the existing zonal jets (the so-called 'Kelvin passive shearing mechanism' - see e.g. Thomson and Mcintyre (2016) and references therein). Such a correlation is found in Jupiter's cloud-level winds (Salyk et al., 2006). The reason for this discrepancy between our results and observations may well be that our mid-to-high latitude jets are maintained by radiative damping, rather than momentum fluxes, meaning that the eddies do not need to pump momentum into the jets. As a result, the power generated by our eddies is $1.65 \times 10^{-8} W kg^{-1}$, which is significantly less than the observed value from Salyk et al. (2006) of $7.1 \times 10^{-5} W kg^{-1}$. These inconsistencies suggest that our radiative damping may well be too large, thus suppressing eddy activity. Inspection of movies of the vorticity field (not shown) suggests that significant passive shearing of vortices is occurring, so reducing the radiative damping significantly may

help to make our model and observations be more consistent. Runs without radiative damping, like the cases shown in figure 8, do show a more significant correlation between $\overline{u'v'}$ and $\overline{u}/d\phi$, suggesting that weaker radiative damping would be a fruitful way forward. Longer radiative damping times are, however, significantly more computationally expensive, and investigation of this limit is left as future work.

One significant caveat to the above statement, however, is that the energy-conversion rates from eddies into zonal-mean kinetic energy implied by the fluxes observed by Salyk et al. (2006) is that it gives a power range that is a significant fraction of Jupiter's thermal emission (Salyk et al., 2006, , and references therein). It has therefore been suggested that such a conversion must be a very shallow phenomenon, and it is therefore not clear what the eddy-to-zonal-mean conversion looks like in a weather-layer integrated sense, which would be more akin to what a one-layer model is representing. It is therefore hard to completely rule out scenarios like that found in our 'realistic' experiments based on the Salyk et al. (2006) measurments, and we plan to compare our results here more closely with three-dimensional Jupiter models in order to fascilitate a more meaningful comparison.

The jets formed at high-latitudes in this case are remarkably zonally-symmetric (not shown) exhibiting Jupiter-like straightness. This is almost certainly because of the strength of the coupling to the straight deep jets.

One final intriguing aspect of these realistic runs is the stability of their zonal-wind profiles with respect to shear instability. The zonal-mean profiles of the potential vorticity Q, shown in figure 9c, indicate that the flow should be unstable to instability via the Charney–Stern criterion, which says that the flow is deemed unstable if $\partial\overline{Q}/\partial\phi$ changes sign in latitude. Interestingly, the flow in this case is close to stability via Arnold's second stability criterion (not shown), which says that a flow is stable if an α can be found such that $(\overline{u}-\alpha)/\overline{q}_y < L_D^2$ (see e.g. Dowling, 1995; Read et al., 2006; Thomson and McIntyre, 2016). However, some of the changes in sign of PV gradient may well be due to the presence of large and strong cyclones and anticyclones sitting in the cyclonic and anticyclonic shear zones at high latitudes (not shown), meaning that the zonal-mean picture may not be applicable. A possible alternative explanation for stability is that the jet spacing at high latitudes is actually $\sim 9L_D$. As discussed in Thomson and McIntyre (2016), this is a valid mechanism for stability as the opposing PV gradients are sufficiently far apart that the counter-propagating Rossby-waves on these gradients cannot 'feel' each other, meaning the phase-locking of such waves, and therefore instability, is suppressed. Further investigation of cases without such large vortices is required to investigate these problems further.

8 | DISCUSSION AND CONCLUSIONS

In this study we have considered the mechanisms of coupling between shallow weather-layer jets and deep zonally-symmetric jet streams in a 1.5-layer shallow-water model set up in a Jupiter-like regime. One of our main results is that radiative damping is a very effective coupling mechanism, although its effectivness is very much a function of L_D. Large values of L_D render radiative damping ineffective, but the smaller values we expect to find on Jupiter are more conclusive to radiative damping being an efficient coupling mechanism. Radiative damping is also most effective at high latitudes, with equatorial flow being relatively unconstrained by radiative processes, consistent with previous studies for Earth and planetary atmospheres (Haynes, 1998; Scott and Polvani, 2007). It is difficult to evaluate how important radiative damping is on the real Jupiter with a shallow-water model of this type, given the highly simplified view of radiative damping compared with a model using full radiative transfer. As a result we are conducting similar investigations of coupling of deep jets with those in the weather-layer with a 3D general circulation model (GCM), also constructed using the Isca framework (Vallis et al., 2018). These runs includes deep-jets that are specified within the bottom layer of a multi-layered atmosphere, much as in the present model.

Without radiative damping, coupling is strongest when n_{Rh} matches the deep-jet spacing, with the latitudinal phases and spacing of the jets matching up in these cases. However, the coupling of this type is not strong enough on its own to stop continually-forced jets from merging, changing their spacing, and thus becoming less coupled. It is interesting, however, that radiative damping brings the upper jets close to the deep jets in spacing terms, which is exactly when the non-radiative coupling becomes most effective. This suggests that, if radiative damping is indeed important on Jupiter, then other coupling mechanisms may also be important. But without radiative damping to bring the jets close together in magnitude and spacing, it is unlikely that the other coupling mechanism would work effectively on its own. It may be, however, that this coupling mechanism, with its apparent resonant behaviour when the deep jet wavenumber is close to n_{Rh} in the upper layer, is stronger in three dimensions, with resonant behaviour existing through each of the layers within the atmosphere. Further work is therefore required with a model that can resolve this vertical structure to see if the resonant behaviour continues.

Intriguingly, there are some cases, notably the case in figure 6, where the presence of the deep jets does not lead to significant jets in high latitudes, but does have a significant impact on the zonality of the flow. This kind of idea may well explain some of the zonality seen in Jupiter's high latitudes despite the lack of strong jets there. Investigating this phenomenan further is a promising avenue for future work.

In our most Jupiter-like simulations, we find strong coupling at high latitudes, and weaker coupling at low latitudes, with the latter resulting in significant equatorial subrotation. The strong coupling at high latitudes is largely thanks to radiative damping, although the lack of eddy-momentum being pumped into the jets (as visualised through the lack of correlation between $d\bar{u}/d\phi$ and $\overline{u'v'}$) suggests that this regime may not be especially realistic. Runs without radiative damping do show a more convincing correlation, suggesting that very weak damping would be a fruitful avenue for future work, although the very long computational times associated mean such a limit is beyond the scope of the present study. The possibility that the deep flows in high latitudes may not couple with jet streams in the weather-layer, but may be involved in creating some of the high-latitude symmetry seen in the polar-vortex crystals, as discussed around figure 6, remains an interesting possibility, and will certainly be explored as part of future work.

The lack of superrotation in low latitudes in our most realistic simulations may well be down to the lack of forcing of large-scale Rossby waves, that would propagate into midlatitudes and break, thus leaving a deficit of westward momentum at low latitudes, and hence superrotation. This lack of projection onto Rossby-wave modes may be down to the small spatial scale of our forcing, or that our forcing forces similar waves at all latitudes, leading to there being no net acceleration of the tropics. Given this uncertainty, alternative forcing scenarios are an avenue for future work. One intriguing possibility is that the small-scale random forcing on the real planet is Jovian moist convection (Ingersoll et al., 2000; Gierasch et al., 2000; Thomson and McIntyre, 2016; O'Neill et al., 2015), which may do a better job at forcing such wavemodes at low latitudes and lead to superrotation, as happened with dry convection in Schneider and Liu (2009); Liu and Schneider (2010, 2011). Investigations representing Jovian moist convection have previously produced equatorial subrotation in Jovian shallow-water models (Showman, 2007), but we plan to take an alternative approach by using the moist shallow-water equations (see e.g. Lambaerts et al., 2011), which should give a more self-consistent view of this process.

If Jupiter's radiative damping is indeed weak, as suggested by our realistic simulations above, then our model here predicts that significant shear could well exist between the weather-layer and the deep jets. With a decay with depth being the very-likely possibility, as inferred from Jupiter's distribution of moist convection Thomson and McIntyre (2016), and in Kaspi et al. (2018). Based on our results, we cannot rule out the possibility that the deep jet profile in reality is very different to what we see in the weather layer, both in terms of jet spacing and magnitude. Indeed, the recent suggestion of Duer et al. (2019), based on inferences about forthcoming time-varying magnetic-field measurments by Juno, suggest that the shear between the weather-layer and deeper-jets might be more vertically confined than

previously described by Kaspi et al. (2018). Our suggestion that there may well be significant vertical shear between the different layers of the Jovian atmosphere may therefore be testable via up-coming Juno measurments. This idea will also need testing in a more comprehensive model, however, with ideas such as downward-control (Haynes et al., 1991) suggesting that any shallow flow would likely form deep overturning cells that would burrow deep into the planet to find frictional dissipation, as in Lian and Showman (2008); Liu and Schneider (2010). GCMs that only extend to 10s of bars are likely not deep enough to answer this question fully, with more updated versions of the deep models of Heimpel et al. (2016) that include weather-layer physics being required.

The fact that our model cannot rule out significant shear between the layers does imply that other deep-flow options may well prove fruitful in understanding Juno's gravitational results, although such possibilities still have to be checked closely for their physical realism in comprehensive models.

ACKNOWLEDGEMENTS

SIT wishes to thank Geoffrey K. Vallis for useful discussions, and to GFDL for making their shallow-water code available online. The code used in the experiments described here is packaged within the Isca modeling framework, and is freely available at `exeter.ac.uk/isca`. The author also thanks two anonymous reviewers, whose questions and clarifications improved the manuscript significantly.

CONFLICT OF INTEREST

The author declares no conflict of interest.

REFERENCES

Adriani, A., Mura, A., Orton, G., Hansen, C., Altieri, F., Moriconi, M. L., Rogers, J., Eichstädt, G., Momary, T., Ingersoll, A. P., Filacchione, G., Sindoni, G., Tabataba-Vakili, F., Dinelli, B. M., Fabiano, F., Bolton, S. J., Connerney, J. E. P., Atreya, S. K., Lunine, J. I., Tosi, F., Migliorini, A., Grassi, D., Piccioni, G., Noschese, R., Cicchetti, A., Plainaki, C., Olivieri, A., O'Neill, M. E., Turrini, D., Stefani, S., Sordini, R. and Amoroso, M. (2018) Clusters of cyclones encircling Jupiter's poles. *Nature*, **555**, 216–219. URL: `http://www.nature.com/doifinder/10.1038/nature25491`.

Brown, S., Janssen, M., Adumitroaie, V., Atreya, S., Bolton, S., Gulkis, S., Ingersoll, A., Levin, S., Li, C., Li, L., Lunine, J., Misra, S., Orton, G., Steffes, P., Tabataba-Vakili, F., Kolmašová, I., Imai, M., Santolík, O., Kurth, W., Hospodarsky, G., Gurnett, D. and Connerney, J. (2018) Prevalent lightning sferics at 600 megahertz near Jupiter's poles. *Nature*, **558**, 87–90. URL: `http://dx.doi.org/10.1038/s41586-018-0156-5http://www.nature.com/articles/s41586-018-0156-5`.

Cho, J. and Polvani, L. (1996) The emergence of jets and vortices in freely evolving, shallow-water turbulence on a sphere. *Physics of Fluids*, **8**, 1531–1552. URL: `http://scitation.aip.org/content/aip/journal/pof2/8/6/10.1063/1.868929`.

Cho, J. Y.-K., de la Torre Juarez, M., Ingersoll, A. P. and Dritschel, D. (2001) A high-resolution, three-dimensional model of Jupiter's Great Red Spot. *Journal of Geophysical Research*, **106**, 5099–5105. URL: `http://www.agu.org/journals/je/je0103/2000JE001287/pdf/2000JE001287.pdf`.

Dowling, T. E. (1995) Estimate of Jupiter's Deep Zonal-Wind Profile from Shoemaker-Levy 9 Data and Arnol'd's Second Stability Criterion. *Icarus*, **117**, 439–442.

Dowling, T. E. and Ingersoll, A. P. (1988) Potential Vorticity and Layer Thickness Variations in the Flow around Jupiter's Great Red Spot and White Oval BC. *Journal of the Atmospheric Sciences*, **45**, 1380–1396.

— (1989) Jupiter's Great Red Spot as a Shallow Water System. *Journal of the Atmospheric Sciences*, **46**, 3256–3278. URL: http://journals.ametsoc.org/doi/abs/10.1175/1520-0469{\%}281989{\%}29046{\%}3C3256{\%}3AJGRSAA{\%}3E2.0.CO{\%}3B2.

Duer, K., Galanti, E. and Kaspi, Y. (2019) Analysis of Jupiter's Deep Jets Combining Juno Gravity and Time-varying Magnetic Field Measurements. *The Astrophysical Journal*, **879**, L22. URL: http://dx.doi.org/10.3847/2041-8213/ab288ehttps://iopscience.iop.org/article/10.3847/2041-8213/ab288e.

ir, F. (1989) Temporal Behavior of Jupiter's Meteorology. *NASA SPECIAL PUBLICATION SERIES*, **NASA-SP-49**, 324–343.

Gal erin, B., Young, R. M., Sukoriansky, S., Dikovskaya, N., Read, P. L., Lancaster, A. J. and Armstrong, D. (2014) Cassini observations reveal a regime of zonostrophic macroturbulence on Jupiter. *Icarus*, **229**, 295–320. URL: http://linkinghub.elsevier.com/retrieve/pii/S0019103513003837.

Gierasch, P., Ingersoll, A., Banfield, D., Ewald, S., Helfenstein, P., Simon-Miller, A., Vasavada, A. R., Breneman, H., Senske, D. and eam, G. (2000) Observation of moist convection in Jupiter's atmosphere. Galileo Imaging Team. *Nature*, **403**, 628–30. URL: http://www.nature.com/nature/journal/v403/n6770/pubmed/403628a0.htmlhttp://dx.doi.org/10.1038/35001017.

Guillot, T. (2005) The Interiors of Giant Planets: Models and Outstanding Questions. *Annual Review of Earth and Planetary ciences*, **33**, 493–530. URL: http://www.annualreviews.org/doi/abs/10.1146/annurev.earth.32.101802.120325.

Hammel, H., Beebe, R., Ingersoll, A., Orton, G., R, M. J., Simon-Miller, A., Chodas, P., Clarke, J. T., De Jong, E., Dowling, T., Harrington, J., Huber, L. F., Karkoschka, E., Santori, C. M., Toigo, A., Yeomans, D. and West, R. (1995) HST imaging of atmospheric phenomena created by the impact of comet Shoemaker-Levy 9. *Science*, **267**, 1288–1296. URL: http://www.sciencemag.org/content/267/5202/1288.short.

Hay es, P., Marks, C. J., McIntyre, M., Shepherd, T. and Shine, K. P. (1991) On the'downward control' of extratropical diabatic rculations by eddy- induced mean zonal forces. *Journal of the Atmospheric Sciences*, **48**. URL: http://www.damtp.cam.ac.uk/user/mem/downward-control-jas91.pdf.

Hay es, P. H. (1998) The latitudinal structure of the quasi-biennial oscillation. *Quarterly Journal of the Royal Meteorological Society*, **124**, 2645–2670.

Heimpel, M., Aurnou, J. and Wicht, J. (2005) Simulation of equatorial and high-latitude jets on Jupiter in a deep convection model. *Nature*, **438**, 193–6. URL: http://www.ncbi.nlm.nih.gov/pubmed/16281029.

M., Gastine, T. and Wicht, J. (2016) Simulation of deep-seated zonal jets and shallow vortices in gas giant atmospheres. *Nature Geosci*, **9**, 19–23. URL: http://dx.doi.org/10.1038/ngeo2601http://10.0.4.14/ngeo2601http://www.ature.com/ngeo/journal/v9/n1/abs/ngeo2601.html{\#}supplementary-information.

Ingersoll, A. P., Gierasch, P. J., Banfield, D. and Vasavada, A. R. (2000) Moist convection as an energy source for the large-scale otions in Jupiter's atmosphere. *Nature*, **403**, 630–632.

Jones, C. A. and Kuzanyan, K. M. (2009) Compressible convection in the deep atmospheres of giant planets. *Icarus*, **204**, 227–238. URL: http://linkinghub.elsevier.com/retrieve/pii/S0019103509002383.

Kaspi, Y., Galanti, E., Hubbard, W. B., Stevenson, D. J., Bolton, S. J., Iess, L., Guillot, T., Bloxham, J., Connerney, J. E. P., Cao, H., Durante, D., Folkner, W. M., Helled, R., Ingersoll, A. P., Levin, S. M., Lunine, J. I., Miguel, Y., Militzer, B., Parisi, M. and Wahl, S. M. (2018) Jupiter's atmospheric jet streams extend thousands of kilometres deep. *Nature*, **555**, 223–226. URL: http://www.nature.com/doifinder/10.1038/nature25793.

Kong, D., Zhang, K., Schubert, G. and Anderson, J. D. (2018) Origin of Jupiter's cloud-level zonal winds remains a puzzle even after Juno. *Proceedings of the National Academy of Sciences*, **115**, 8499–8504. URL: http://www.pnas.org/lookup/doi/10.1073/pnas.1805927115.

Lambaerts, J., Lapeyre, G. and Zeitlin, V. (2011) Moist versus Dry Barotropic Instability in a Shallow-Water Model of the Atmosphere with Moist Convection. *Journal of the Atmospheric Sciences*, **68**, 1234–1252. URL: http://journals.ametsoc.org/doi/abs/10.1175/2011JAS3540.1.

Lian, Y. and Showman, A. P. (2008) Deep jets on gas-giant planets. *Icarus*, **194**, 597–615. URL: http://dx.doi.org/10.1016/j.icarus.2007.10.014.

Liu, J. and Schneider, T. (2010) Mechanisms of Jet Formation on the Giant Planets. *Journal of the Atmospheric Sciences*, **67**, 3652–3672. URL: http://journals.ametsoc.org/doi/abs/10.1175/2010JAS3492.1.

— (2011) Convective Generation of Equatorial Superrotation in Planetary Atmospheres. *Journal of the Atmospheric Sciences*, **68**, 2742–2756. URL: http://journals.ametsoc.org/doi/abs/10.1175/JAS-D-10-05013.1.

Scus, P. S. and Shetty, S. (2011) Jupiter's zonal winds: are they bands of homogenized potential vorticity organized as a monotonic staircase? *Philosophical Transactions of the Royal Society A: Mathematical, Physical and Engineering Sciences*, **369**, 771–795. URL: http://www.ncbi.nlm.nih.gov/pubmed/21242133http://rsta.royalsocietypublishing.org/cgi/doi/10.1098/rsta.2010.0299.

O'Neill, M. E., Emanuel, K. a. and Flierl, G. R. (2015) Polar vortex formation in giant-planet atmospheres due to moist convection. *Nature Geoscience*, **8**, 523–526. URL: http://www.nature.com/doifinder/10.1038/ngeo2459.

Pirraglia, J. (1984) Meridional energy balance of Jupiter. *Icarus*, **59**, 169–176. URL: https://linkinghub.elsevier.com/retrieve/pii/0019103584900204.

Porco, C. C., West, R. a., McEwen, A., Del Genio, A. D., Ingersoll, A. P., Thomas, P., Squyres, S., Dones, L., Murray, C. D., Johnson, T. V., Burns, J. a., Brahic, A., Neukum, G., Veverka, J., Barbara, J. M., Denk, T., Evans, M., Ferrier, J. J., Geissler, P., Helfenstein, P., Roatsch, T., Throop, H., Tiscareno, M. and Vasavada, A. R. (2003) Cassini imaging of Jupiter's atmosphere, satellites and rings. *Science (New York, N.Y.)*, **299**, 1541–7. URL: http://www.ncbi.nlm.nih.gov/pubmed/12624258.

Read, P. L., Gierasch, P. J., Conrath, B. J., Simon-Miller, A., Fouchet, T. and Yamazaki, Y. H. (2006) Mapping potential-vorticity dynamics on Jupiter. I: Zonal-mean circulation from Cassini and Voyager 1 data. *Quarterly Journal of the Royal Meteorological Society*, **132**, 1577–1603. URL: http://doi.wiley.com/10.1256/qj.05.34.

Salyk, C., Ingersoll, A. P., Lorre, J., Vasavada, A. and Del Genio, A. D. (2006) Interaction between eddies and mean flow in Jupiter's atmosphere: Analysis of Cassini imaging data. *Icarus*, **185**, 430–442. URL: http://linkinghub.elsevier.com/retrieve/pii/S0019103506002727.

Schneider, T. and Liu, J. (2009) Formation of Jets and Equatorial Superrotation on Jupiter. *Journal of the Atmospheric Sciences*, **66**, 579–601. URL: http://journals.ametsoc.org/doi/abs/10.1175/2008JAS2798.1.

Scott, R. K. and Polvani, L. M. (2007) Forced-Dissipative Shallow-Water Turbulence on the Sphere and the Atmospheric Circulation of the Giant Planets. *Journal of the Atmospheric Sciences*, **64**, 3158–3176. URL: http://journals.ametsoc.org/doi/abs/10.1175/JAS4003.1.

Shetty, S., Asay-Davis, X. S. and Marcus, P. S. (2007) On the Interaction of Jupiter's Great Red Spot and Zonal Jet Streams. *Journal of the Atmospheric Sciences*, **64**, 4432–4444. URL: http://journals.ametsoc.org/doi/abs/10.1175/2007JAS2097.1.

Shetty, S. and Marcus, P. S. (2010) Changes in Jupiter's Great Red Spot (1979–2006) and Oval BA (2000–2006). *Icarus*, **210**, 182–201. URL: http://linkinghub.elsevier.com/retrieve/pii/S0019103510002484.

Showman, A. P. (2007) Numerical Simulations of Forced Shallow-Water Turbulence: Effects of Moist Convection on the Large-Scale Circulation of Jupiter and Saturn. *Journal of the Atmospheric Sciences*, **64**, 3132–3157. URL: http://journals.ametsoc.org/doi/abs/10.1175/JAS4007.1.

Tabataba-Vakili, F., Rogers, J., Eichstädt, G., Orton, G., Hansen, C., Momary, T., Sinclair, J., Giles, R., Caplinger, M., Ravine, M. and Bolton, S. (2020) Long-term tracking of circumpolar cyclones on Jupiter from polar observations with JunoCam. *Icarus*, **335**, 113405. URL: https://linkinghub.elsevier.com/retrieve/pii/S0019103519302751.

Theiss, J. (2004) Equatorward Energy Cascade, Critical Latitude, and the Predominance of Cyclonic Vortices in Geostrophic Turbulence. *Journal of Physical Oceanography*, **34**, 1663–1678.

Thomson, S. I. (2015) *A new model of Jupiter's jet streams and the effects of moist convection*. Ph.D. thesis.

Thomson, S. I. and McIntyre, M. E. (2016) Jupiter's Unearthly Jets: A New Turbulent Model Exhibiting Statistical Steadiness without Large-Scale Dissipation*. *Journal of the Atmospheric Sciences*, **73**, 1119–1141. URL: http://journals.ametsoc.org/doi/10.1175/JAS-D-14-0370.1.

Vallis, G. K. (2017) *Atmospheric and Oceanic Fluid Dynamics*. Cambridge: Cambridge University Press, second edi edn. URL: http://ebooks.cambridge.org/ref/id/CBO9781107588417.

Vallis, G. K., Colyer, G., Geen, R., Gerber, E., Jucker, M., Maher, P., Paterson, A., Pietschnig, M., Penn, J. and Thomson, S. I. (2018) Isca, v1.0: a framework for the global modelling of the atmospheres of Earth and other planets at varying levels of complexity. *Geoscientific Model Development*, **11**, 843–859. URL: https://www.geosci-model-dev.net/11/843/2018/.

Vallis, G. K., Gerber, E. P., Kushner, P. J. and Cash, B. a. (2004) A Mechanism and Simple Dynamical Model of the North Atlantic Oscillation and Annular Modes. *Journal of the Atmospheric Sciences*, **61**, 264–280.

Walterscheid, R. (2000) Wave Disturbances from the Comet SL-9 Impacts into Jupiter's Atmosphere. *Icarus*, **145**, 140–146. URL: http://dx.doi.org/10.1006/icar.1999.6334.

Williams, G. (2003) Jovian dynamics. Part III: Multiple, migrating, and equatorial jets. *Journal of the atmospheric sciences*, 1270–1296. URL: http://journals.ametsoc.org/doi/full/10.1175/1520-0469(2003)60{\%}3C1270:JDPIMM{\%}3E2.0.CO{\%}3B2.

Young, R. M. B. and Read, P. L. (2017) Forward and inverse kinetic energy cascades in Jupiter's turbulent weather layer. *Nature Physics*, **11**. URL: http://www.nature.com/doifinder/10.1038/nphys4227.